Available online at www.sciencedirect.com
SCIENCE DIRECT
Journal of Sound and Vibration 295 (2006) 388–406
JOURNAL OF SOUND AND VIBRATION
www.elsevier.com/locate/jsvi

Element-free Galerkin method for static and dynamic analysis of spatial shell structures

L. Liu*, L.P. Chua, D.N. Ghista

School of Mechanical and Aerospace Engineering, Nanyang Technological University, North Spine (N3), level 2, 50 Nanyang Avenue, Singapore 639798, Singapore

Received 2 December 2004; received in revised form 16 January 2006; accepted 20 January 2006
Available online 20 March 2006

Abstract

The implementation of the element free Galerkin method (EFG) for static and free vibration analysis of general shell structures is presented in this paper. The formulation of the discrete system equations is derived from the governing equations of stress resultant geometrically exact shell theory based on the Cosserat surface. A discrete singularity-free mapping between the five- and the six-degrees-of-freedom formulation is constructed by exploiting the geometry connection between the orthogonal group and the unit sphere. Moving least-squares approximation is used in both the construction of shape functions based on arbitrarily distributed nodes as well as in the surface approximation of general spatial shell geometry. Discrete system equations are obtained by incorporating these interpolations into the Galerkin weak form. The formulation is verified through numerical examples of static stress analysis and frequency analysis of spatial shell structures. The phenomena of shear locking and membrane locking are illustrated by showing the membrane and shear energy as fractions of the total energy. Essential boundary conditions are efficiently imposed through a penalty technique for both static analysis and frequency analysis. The formulation is tested on several benchmark problems and the results compare favorably with closed-form solutions and that of finite element analyses.

1. Introduction

The numerical analysis of shell structures has always been a challenge in applied mechanics. In the last three decades, theoretical models have been developed and applied to various practical problems [1]. It should be noted that the shell asymptotic stiffness (as the thickness tend to zero), may vary depending on the shell geometry, the loads and the boundary conditions [2–5]. It has been proposed that when the thickness of shells becomes small, shells fall into dramatically different categories, namely bending-dominated (when the stiffness of the structure is of order ε^3 as $\varepsilon \to 0$ (ε being the shell thickness), most of the elastic energy is typical stored in the bending part), membrane-dominated structures (when the stiffness of the structure is of order ε as $\varepsilon \to 0$, most of the elastic energy is carried by membrane term), and intermediate states (in which neither the bending nor the membrane one asymptotically dominates). Carrera [6,7] presented an overview of available theories

*Corresponding author. Tel.: +65 6790 6174; fax: +65 6790 1459.
E-mail address: MLLIU@ntu.edu.sg (L. Liu).

0022-460X/$ - see front matter © 2006 Elsevier Ltd. All rights reserved.
doi:10.1016/j.jsv.2006.01.015

and finite elements that have been developed for shell structures. He summarized the various approaches available in computational shell analysis: 3-D elasticity theory, continuum based methods, axiomatic and asymptotic 2-D theories, classical and mixed formulations, etc. Then he proposed a unified description of several modeling based on displacements and transverse stress assumptions. There are advantages in using shell theories for structures instead of the governing equations for general 3-D solids, which enable an insight into the structure of the equations involved independently. Eriksen and Truesdell [8] initiated the direct approach in the construction of shell theories by considering the shell as a surface with oriented directors. They were inspired by the concept of a Cosserat continuum by which, in addition to the displacement field and independent of it, rotational degrees of freedom (dof) are assigned to every point of the continuum. Simo and Fox [9] proposed a stress-resultant-based geometrically exact shell model that is formulated entirely in terms of stress resultants and is essentially equivalent to a one director inextensible Cosserat surface. There are two important features in the above approaches: One is that the construction of the interpolants for the reference director and the linearized director fields preserve the kinematic structure of the theory; another is that the transformation from six to 5 dof formulation is described by a unique orthogonal transformation that maps the inertial frame onto an orthonormal director frame without drill.

The finite element method (FEM) remains the most popular numerical technique as evident from numerous publications since the 1970s. However, FEM requires the design of meshes, which is an extremely tedious and time-consuming process. In light of decreasing computer costs and increasing manpower costs, mesh-free methods present an attractive alternative to FEM, especially for shell structures that are very complex both in the field variable expression and the geometry representation. Mesh-free methods developed in recent year allow sufficient flexibility in customizing the approximation function of desired smoothness, accuracy or special characteristics of particular engineering and scientific problems. The satisfaction of the C^1 (C^1 means that the first derivative of displacement fields is continuous) continuity requirements of the Kirchhoff plate and shell problems are easily achieved using moving least squares (MLS) approximation since it requires only C^1 weights. Despite of these attractive features, several authors have reported locking difficulties in constrained problems using mesh-free methods.

It has been established that the shear locking phenomenon results from an inconsistency between the rotation and the transverse displacement fields and the membrane locking phenomenon takes place due to the different orders of magnitude for the membrane and bending strains when the shell is thin. When the shell thickness decreases, shear locking and membrane locking arise because of the inability of shell to achieve deformed states in which the transverse shear strain and membrane strain vanish throughout the structure. Therefore a modification of the membrane energy term is needed in the bending-dominated shells structures to avoid locking effects, however, a modification of membrane energy in membrane-dominated shells may cause undesirable numerical instabilities [3,4]. For the element free Garberkin (EFG) method, it allows the definition of smooth and consistent approximations for rotation and displacements. Donning and Liu [10] proposed the matching field approach to eliminate the shear locking phenomenon for beams, they discovered that the approximate slope field may be matched with that of the approximate rotation field by the consistent property of cardinal spline functions constructed over uniformly spaced arrangements of nodes. Kanok-Nukulchai et al. [11] proposed a modified version of the element-free Galerkin (MEFG) to apply the matching field approach on the bending problems such as beams and plates in conjunction with the EFG method. The shape functions for rotation are constructed from the corresponding partial derivatives of the shape functions for displacement. This leads to a complete absence of transverse shear locking and a high degree of accuracy for EFG analysis regardless of the slenderness ratio of the respective beams and plates. However, the design of a numerical procedure that is general and optimal for all categories is very difficult, and mathematical analysis of available numerical schemes hardly exist . Thus, it is crucial to have available appropriate numerical test problems, and use these in a judicious manner to evaluate the capability of a numerical scheme [12–15]. In the paper, the matching field approach and high-order basis functions are used in order to avoid shear and membrane locking. The variation in membrane energy and shear energy are presented to illustrate the features of membrane and shear locking.

Krysl and Belytschko [16] implemented the EFG method for thin shells as MLS approximation can easily produce C^1 continuous displacement fields to satisfy the Kirchhoff hypothesis. Li et al. [17] utilized RKPM to simulate large deformation of thin shell structures using the window function to construct highly smoothed shape functions. Noguchi et al. [18] applied the EFG method to analyze the general shell based on the total

Lagrangian method. In this paper, shell formulation based on Cosserat surface theory using the EFG method is presented. There are only 5 dof assigned to every point of the shell. The surface approximation of the geometry of an arbitrary curved surface is constructed using MLS approximation. Different types of basis functions are adopted to avoid membrane and shear locking. In the present formulation, the penalty method is used to impose the essential boundary conditions, which is applicable not only to the static deflection analysis, but also to the free vibration analysis. The discrete system equation so derived has a simple form as that in conventional FEM and is more efficient than orthogonal transform method [19]. The outline of the paper is as follows. In Section 2, a short account of the numerical formulation of the geometrically exact shell theory is given. First, the definition of configuration space, stress resultant, stress couples and constitutive equations adopted in the formulation are described. Then the equations of virtual work for static analysis and equations for imposing the boundary condition by the Lagrange Multipliers is introduced and the discrete equations are derived. In Section 3, the results of several shell benchmark tests are presented to validate the proposed method. Finally, conclusions are drawn in Section 4. In Appendix A, the derivation of the EFG shape function from MLS approximation method is briefly reviewed.

2. Governing equations for general shell

2.1. The configuration space and deformation gradient

A continuum is termed classical if the displacement field completely describes the deformation process. Hence, every point of a classical continuum is associated with 3 dof. On the contrary, the Cosserat continuum, which is the simplest possible continuum of a wide class of continua to be considered non-classical, is characterized by the fact that to every point of the continuum the displacements and rotations are assigned.

The shell theory is based on the assumption that all governing equations describing shell deformation can be derived by considering a Cosserat surface with a displacement as well as a rotation field are attached. The shell theory presented here is based on the idea that a thin 3-D classical continuum can be directly modeled as a 2-D non-classical continuum. A 2-D Cosserat continuum in the paper is referred to as a Cosserat surface.

The set Re is defined to state precisely the basic kinematic assumption [20]

$$\mathrm{Re} := \left\{(\boldsymbol{\varphi}, \mathbf{t}) : \mathbb{A} \subset \mathbb{R}^2 \to \mathbb{R}^3 \times S^2\right\}. \tag{1}$$

Here $\mathbb{A} \subset \mathbb{R}^2$ is an open set with smooth boundary $\partial\mathbb{A}$, compact closure $\overline{\mathbb{A}}$, and points denoted $\xi \in \mathbb{A}$. The following expressing is set

$$\xi = \xi^1 E_1 + \xi^2 E_2 \quad \left(\xi^1, \xi^2\right) \in \mathbb{R}^2. \tag{2}$$

The basic kinematic assumption is that of an inextensible one-direct Cosserat surface. Accordingly, the Gauss intrinsic coordinates are used to describe the configuration of the shell, any configuration of the shell is described by a pair $(\boldsymbol{\varphi}, \mathbf{t}) \in \mathrm{Re}$, where the map $\boldsymbol{\varphi} : \mathbb{A} \to \mathbb{R}^3$ defines the position of the middle surface of the shell and the map $\mathbf{t} : \mathbb{A} \to S^2$ defines a unit vector field at each point of the surface, refer to the director field.

Hence, the configuration of the shell is defined as

$$\mathfrak{A} = \left\{\mathbf{x} \in \mathbb{R}^3 : \mathbf{x} = \boldsymbol{\varphi}(\xi^1, \xi^2) + \xi \mathbf{t}(\xi^1, \xi^2) \quad \text{with} \quad \xi^1, \xi^2 \in \mathbb{A} \quad \text{and} \quad \xi \in \left\langle h^-, h^+ \right\rangle\right\}. \tag{3}$$

Here, (h^-, h^+) are the distances of the "lower" and "upper" surfaces of the shell measured from the shell mid-surface, $\mathbf{t}(\xi^1, \xi^2) \in S^2$.

The convected basis vectors g_I are defined as

$$\nabla \mathbf{x} = \frac{\partial \mathbf{x}}{\partial \xi^I} \otimes \mathbf{E}^I \equiv \mathbf{g}_I \otimes \mathbf{E}^I. \tag{4}$$

Here, ∇ denotes gradient, $\otimes$ denotes tensor product and $\mathbf{E}$ denotes inertial basis. In addition to the convected basis, a contravariant basis $\mathbf{g}^I$ can be obtained from the standard relation $\mathbf{g}^I \cdot \mathbf{g}_J = \delta^I_J$.

The mid-surface is defined by the differential two form

$$\mathrm{d}\mathbb{A} = \boldsymbol{\varphi}_{,1} \times \boldsymbol{\varphi}_{,2} \mathrm{d}\xi^1 \mathrm{d}\xi^2, \tag{5}$$

where " $\times$ " denotes vector cross-product. The determinants of the tangent maps in the deformed and reference configuration will be denoted subsequently as j and j^0, respectively, with $\bar{j}$ and $\bar{j}^0$ denoting the Jacobians on the mid-plane surface;

$$j = \det[\nabla \mathbf{x}], \quad j^0 = \det\left[\nabla \mathbf{x}^0\right], \quad \bar{j} = j\big|_{\xi=0}, \quad \bar{j}^0 = j^0\big|_{\xi=0}, \tag{6}$$

where the superscript "0" is used to denote quantities in the reference configuration.

In addition to the fixed inertial frame, two reference frames on the mid-surface are defined to play an important role in the following formula. The reference frames on the mid-surface are illustrated in Fig. 1. The surface-convected frame, which spans the tangent space to the mid-surface, is defined as $a_\alpha = \boldsymbol{\varphi}_{,\alpha} (\alpha = 1, 2)$. Hence, the first fundamental form on the reference surface is

$$\boldsymbol{a} = a_{\alpha\beta} \boldsymbol{a}^\alpha \otimes \boldsymbol{a}^\beta, \quad a_{\alpha\beta} = \boldsymbol{\varphi}_{,\alpha} \cdot \boldsymbol{\varphi}_{,\beta}. \tag{7}$$

Here, $a^I (I = 1, 2)$ denotes the dual surface convected basis through the standard relation $\boldsymbol{a}^I \cdot \boldsymbol{a}_J = \delta^I_J$ and " $\cdot$ " denotes dot product.

The director orthogonal frame is defined as

$$\mathbf{t}_\alpha = \boldsymbol{\Psi} \mathbf{E}_\alpha \ (\alpha = 1, 2), \quad \mathbf{t}_3 = \boldsymbol{\psi} \mathbf{E}_3 = \mathbf{t}. \tag{8}$$

Here, $\{\mathbf{t}_I\}$ is the orthonormal basis, ${S_E}^2$ is the set of rotations whose rotation axis is perpendicular to $\mathbf{E}$, $\boldsymbol{\psi} : \mathbb{A} \subset \mathbb{R}^2 \to S^2_E$ is the orthogonal transformation, which could be expressed as

$$\boldsymbol{\Psi} = (\mathbf{t} \cdot \mathbf{E})\mathbf{I} + [\widehat{\mathbf{E} \times \mathbf{t}}] + \frac{1}{1 + \mathbf{t} \cdot \mathbf{E}} (\mathbf{E} \times \mathbf{t}) \otimes (\mathbf{E} \times \mathbf{t}). \tag{9}$$

Here, $\mathbf{I}$ is the 3×3 unit matrix. $[\widehat{\mathbf{E} \times \mathbf{t}}]$ is the skew-symmetric tensor while $[\mathbf{E} \times \mathbf{t}]$ is the corresponding axial vector.

2.2. Stress resultants and stress couples

A section in the current configuration is described [20]

$$\mathfrak{A}^\alpha = \left\{ \mathbf{x} \in \square^3 : \mathbf{x} = \mathbf{x}|_{\xi^\alpha = \text{const}} \right\}, \quad \alpha = 1, 2. \tag{10}$$

The stress resultants and resultant couples are defined as

$$\mathbf{n}^\alpha = \left(\bar{j}\right)^{-1} \int_{h^-}^{h^+} \boldsymbol{\sigma} \mathbf{g}^\alpha j \, \mathrm{d}\xi, \quad \alpha = 1, 2 \tag{11}$$

and

$$\mathbf{m}^\alpha = \left(\bar{j}\right)^{-1} \int_{h^-}^{h^+} (\mathbf{x} - \boldsymbol{\varphi}) \times \boldsymbol{\sigma} \mathbf{g}^\alpha j \, \mathrm{d}\xi, \quad \alpha = 1, 2. \tag{12}$$

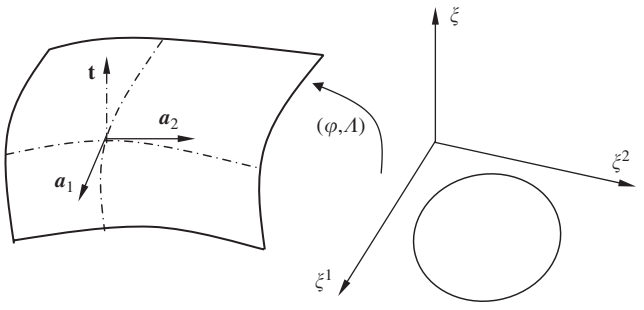

Fig. 1. Reference frames on the mid-surface.

The through thickness stress resultant is denoted by

$$\boldsymbol{l} = (\bar{j})^{-1} \int_{h^-}^{h^+} \boldsymbol{\sigma} \mathbf{g}^3 j \, \mathrm{d}\xi. \tag{13}$$

The director stress couple $\tilde{\mathbf{m}}^\alpha$ can also be defined by

$$\tilde{\mathbf{m}}^\alpha = (\bar{j})^{-1} \int_{h^-}^{h^+} \xi \boldsymbol{\sigma} \mathbf{g}^\alpha j \, \mathrm{d}\xi. \tag{14}$$

The effective membrane and effective shear resultant forces, which are denoted by $\tilde{\boldsymbol{n}} = \tilde{n}^{\beta\alpha} \boldsymbol{a}_\beta \otimes \boldsymbol{a}_\alpha$ and $\tilde{\mathbf{q}} = \tilde{q}^\alpha \varphi_{,\alpha}$ respectively, can be defined by the following relations

$$\tilde{n}^{\beta\alpha} = n^{\beta\alpha} - \lambda^\beta_\mu \tilde{m}^{\alpha\mu} \tag{15}$$

and

$$\tilde{q}^\alpha = q^\alpha - \lambda^3_\mu \tilde{m}^{\alpha\mu}. \tag{16}$$

Here, $\mathbf{t}_{,\alpha} = \lambda^\chi_\alpha \boldsymbol{\varphi}_{,\chi} + \lambda^3_\alpha \mathbf{t}$. The direct stress couple can be denoted by $\tilde{\mathbf{m}} = \tilde{m}^{\beta\alpha} \boldsymbol{a}_\beta \otimes \boldsymbol{a}_\alpha$.

2.3. Linearization

Making use of the definition of spatial tensors, the corresponding linearized strain measures are defined relative to the dual spatial surface basis as

$$\varepsilon_{\alpha\beta} = \frac{1}{2}\left(\boldsymbol{\varphi}^0_{,\alpha} \cdot \mathbf{u}_{,\beta} + \boldsymbol{\varphi}^0_{,\beta} \cdot \mathbf{u}_{,\alpha}\right),$$

$$\gamma_\alpha = \left(\boldsymbol{\varphi}^0_{,\alpha} \cdot \Delta\mathbf{t} + \mathbf{u}_{,\alpha} \cdot \mathbf{t}^0\right)$$

and

$$\rho_{\alpha\beta} = \frac{1}{2}\left(\boldsymbol{\varphi}^0_{,\alpha} \cdot \Delta\mathbf{t}_{,\beta} + \boldsymbol{\varphi}^0_{,\beta} \cdot \Delta\mathbf{t}_{,\alpha} + \mathbf{u}_{,\alpha} \cdot \mathbf{t}^0_{,\beta} + \mathbf{u}_{,\beta} \cdot \mathbf{t}^0_{,\alpha}\right). \tag{17}$$

Here, only the symmetric part of the bending strain measure is considered.

The incremental spatial rotation vector $\Delta\mathbf{t}$ can be defined as

$$\Delta\mathbf{t} = \overline{\boldsymbol{\Psi}} \cdot \Delta\mathbf{T} \tag{18}$$

Here, $\Delta\mathbf{T} = \Delta T^1 \mathbf{E}_1 + \Delta T^2 \mathbf{E}_2$, which means that the drill degree of freedom is automatically excluded. $\overline{\boldsymbol{\Psi}}$ is a (3×2) matrix obtained by deleting the third column of $\boldsymbol{\Psi}$ giving

$$\overline{\boldsymbol{\Psi}} = [\mathbf{t}_1 \mathbf{t}_2] = \begin{bmatrix} \Psi_{11} & \Psi_{12} \\ \Psi_{21} & \Psi_{22} \\ \Psi_{31} & \Psi_{32} \end{bmatrix}. \tag{19}$$

2.4. Constitutive equations

For isotropic elastic shell structures, the constitutive relations for the effective membrane stress $\tilde{\mathbf{n}}$ and the stress couple resultant $\tilde{\mathbf{m}}$ are written as

$$\begin{Bmatrix} \tilde{n}^{11} \\ \tilde{n}^{22} \\ \tilde{n}^{12} \end{Bmatrix} = \frac{Eh}{1-\nu^2} \mathbf{C} \begin{Bmatrix} \varepsilon_{11} \\ \varepsilon_{22} \\ 2\varepsilon_{12} \end{Bmatrix} = \mathbf{D}_1 \begin{Bmatrix} \varepsilon_{11} \\ \varepsilon_{22} \\ 2\varepsilon_{12} \end{Bmatrix}$$

and

$$\begin{Bmatrix} \tilde{m}^{11} \\ \tilde{m}^{22} \\ \tilde{m}^{12} \end{Bmatrix} = \frac{Eh^3}{12(1-v^2)}\mathbf{C}\begin{Bmatrix} \rho_{11} \\ \rho_{22} \\ 2\rho_{12} \end{Bmatrix} = \mathbf{D}_2\begin{Bmatrix} \rho_{11} \\ \rho_{22} \\ 2\rho_{12} \end{Bmatrix}, \tag{20}$$

where the matrix $\mathbf{C}$ is given by

$$\mathbf{C} = \begin{bmatrix} (a^{011})^2 & \left(va^{011}a^{022} + (1-v)(a^{012})^2\right) & a^{011}a^{012} \\ & (a^{022})^2 & a^{022}a^{012} \\ \text{symm} & & \frac{1}{2}\left((1+v)(a^{012})^2 + (1-v)a^{011}a^{022}\right) \end{bmatrix}. \tag{21}$$

Here, $a^{0\alpha\beta}$ are the components of the first fundamental form in the dual basis, E is the Young's modulus, v is Poisson's ratio, h is the thickness of shell. The shear stress resultants $\tilde{\mathbf{q}}$ is given by

$$\tilde{\mathbf{q}} = \begin{Bmatrix} \tilde{q}^1 \\ \tilde{q}^2 \end{Bmatrix} = \kappa Gh\begin{Bmatrix} \gamma^1 \\ \gamma^2 \end{Bmatrix} = D_3\begin{Bmatrix} \gamma^1 \\ \gamma^2 \end{Bmatrix}. \tag{22}$$

Here, κ is the shear reduction coefficient, G is the shear modulus. The constitutive equations for the resultant director couple are given in terms of the symmetrical part of $\tilde{m}^{\alpha\beta}$. The skew-symmetric part of $\tilde{m}^{\alpha\beta}$ is assumed to be zero.

2.5. Principle of virtual work

By making use of the basic kinematic assumption equation given by Eq. (3), the weak form of the governing equation for the shells under static load is

$$\boldsymbol{W}_{\text{Sta}}(\delta\mathbf{x}) = \int_{\mathbb{A}} \left[\tilde{n}^{\beta\alpha}\cdot\delta\varepsilon_{\beta\alpha} + \tilde{m}^{\beta\alpha}\cdot\delta\kappa_{\beta\alpha} + \tilde{q}^{\alpha}\cdot\delta\gamma_{\alpha}\right]\mathrm{dRe} - \boldsymbol{W}_{\text{ext}}(\delta\mathbf{x}). \tag{23}$$

Here, $\mathrm{dRe} = \bar{j}\,\mathrm{d}\xi^1\,\mathrm{d}\xi^2$ is the current surface measure. $\boldsymbol{W}_{\text{ext}}$ is the virtual work of the external loading given by

$$\boldsymbol{W}_{\text{ext}} = \int_{\mathbb{A}} [\bar{\mathbf{n}}\cdot\delta\boldsymbol{\varphi} + \bar{\tilde{\mathbf{m}}}\cdot\delta\tilde{\mathbf{t}}]\,\mathrm{dRe} + \int_{\partial_n\mathbb{A}} \bar{\mathbf{n}}\cdot\delta\boldsymbol{\varphi}\bar{j}\,\mathrm{d}s + \int_{\partial_m\mathbb{A}} \bar{\tilde{\mathbf{m}}}\cdot\delta\mathbf{t}\bar{j}\,\mathrm{d}s, \tag{24}$$

where $\bar{\mathbf{n}}$ is the applied resultant force per unit length and $\bar{\tilde{\mathbf{m}}}$ is the applied direct couple per unit length. $\bar{\mathbf{n}}$ and $\bar{\tilde{\mathbf{m}}}$ Z are the prescribed resultant force and the prescribed director couple on the boundaries $\partial_n\mathbb{A}$ and $\partial_m\mathbb{A}$, respectively.

As the Kronecker delta function property is not satisfied at each node by the MLS shape function, the essential boundary conditions cannot be imposed directly as in FEM. In the paper, the essential boundary conditions are enforced through an additional boundary condition term in the variational form of the static–elastic equilibrium equation. When the penalty method is utilized to impose the essential boundary conditions, the modified variational form is written as

$$\boldsymbol{W}_{\text{Sta}}(\delta\mathbf{x}) + \int_{\mathbb{A}_u} \boldsymbol{\alpha}\cdot(\mathbf{u}-\bar{\mathbf{u}})\delta\mathbf{u}\,\mathrm{d}s = 0. \tag{25}$$

Here, $\mathbf{u}$ and $\bar{\mathbf{u}}$ are the nodal vector and prescribed vector corresponding to one of the dof in the displacement or rotation vector on the surface Re_u. $\boldsymbol{\alpha}$ is a diagonal matrix of penalty coefficients which are usually very large numbers.

For free vibration analysis of spatial shells, in order to produce a positive-definite stiffness matrix with smallest dimension for the eigenvalue equation in computing natural frequencies, the discrete system equation and the boundary condition equation are formulated separately. The variational form of the dynamical

undamped equilibrium equation can be written as

$$\int_{\mathbb{A}} \left[\tilde{n}^{\beta\alpha} \cdot \delta\varepsilon_{\beta\alpha} + \tilde{m}^{\beta\alpha} \cdot \delta\kappa_{\beta\alpha} + \tilde{q}^{\alpha} \cdot \delta\gamma_{\alpha}\right] \mathrm{d}\mathrm{Re} + \int_{\mathrm{Re}} \delta\mathbf{u} \cdot \rho\ddot{\mathbf{u}}\, \mathrm{d}\mathrm{Re} - \boldsymbol{W}_{\mathrm{ext}}(\delta\mathbf{x}) = 0, \tag{26}$$

where ρ is the mass density of the material. The weak form equilibrium equation with the penalty technique employed on the essential boundary conditions is given as

$$\int_{\mathbb{A}} \left[\tilde{n}^{\beta\alpha} \cdot \delta\varepsilon_{\beta\alpha} + \tilde{m}^{\beta\alpha} \cdot \delta\kappa_{\beta\alpha} + \tilde{q}^{\alpha} \cdot \delta\gamma_{\alpha}\right] \mathrm{d}Re + \int_{\mathrm{Re}} \delta\mathbf{u} \cdot \rho\ddot{\mathbf{u}}\mathrm{d}\mathrm{Re} - \boldsymbol{W}_{\mathrm{ext}}(\delta\mathbf{x}) + \int_{\mathbb{A}_u} \boldsymbol{\alpha} \cdot (\mathbf{u} - \overline{\mathbf{u}})\delta\mathbf{u}\, \mathrm{d}s = 0. \tag{27}$$

The penalty term to impose essential boundary conditions in Eq. (27) can be discretized to give

$$\boldsymbol{\alpha} \int_{\mathbb{A}_u} \mathbf{u} \cdot \delta\mathbf{u}\, \mathrm{d}s = \sum_{I=1}^{m} \delta\tilde{\mathbf{u}}^{\mathrm{T}} \boldsymbol{\alpha}\boldsymbol{\Phi}_I \boldsymbol{\Phi}_I^{\mathrm{T}} \tilde{\mathbf{u}} \tag{28}$$

and

$$\boldsymbol{\alpha} \int_{\mathbb{A}_u} \overline{\mathbf{u}} \cdot \delta\mathbf{u}\, \mathrm{d}s = \sum_{I=1}^{m} \delta\tilde{\mathbf{u}}^{\mathrm{T}} \overline{\mathbf{u}}_I \boldsymbol{\alpha}\boldsymbol{\Phi}_I, \tag{29}$$

where m is the number of sampling points for integration on surface $\mathbb{A}_u$ and $\tilde{\mathbf{u}}$ is the nodal vector corresponding to a dof in the translation and rotation fields. The penalty matrix in Eq. (28) and the penalty vector in Eq. (29) are assembled in the stiffness matrix and the external force vector, respectively.

2.6. Surface approximation

The MLS technique for surface approximation of general shells is applied in this paper in a consistent manner as in the interpolation of displacement fields. Therefore, the surface approximation is described by

$$\boldsymbol{\varphi}(\zeta) = \phi_I(\zeta)\mathbf{x}_I, \tag{30}$$

where ζ is the parameterization of the surface. A deficiency of this approximation is that the constructed surface does not pass through the prescribed points unlike that of FEM. However, since the polygonalization of surfaces is usually available, curved subsections can be mapped onto flat surfaces. The nodes of FE meshes can act as discrete EFG nodes and the parameterization of the surface ζ can be carried out in a similar manner to the parameterization defined by standard FE interpolation on FE meshes.

2.7. Discrete equation

The displacement vector $\mathbf{u}$ and incremental rotation vector $\Delta\mathbf{t}$ can be expressed in the global Cartesian basis $\mathbf{E}_K$ as

$$\mathbf{u}(\zeta) = \sum_{I=1}^{m} \phi_I(\zeta)[U_I\mathbf{E}_1 + V_I\mathbf{E}_2 + W_I\mathbf{E}_3] = \sum_{I=1}^{m} \phi_I(\zeta)u_I \tag{31}$$

and

$$\Delta\mathbf{t}(\zeta) = \overline{\boldsymbol{\psi}} \cdot \Delta\mathbf{T} = \overline{\boldsymbol{\psi}} \cdot \sum_{I=1}^{m} \phi_I(\zeta)\left[(\Delta T_1)_I\mathbf{E}_1 + (\Delta T_2)_I\mathbf{E}_2\right] = \overline{\boldsymbol{\psi}} \cdot \sum_{I=1}^{m} \phi_I(\zeta)\Delta T_I, \tag{32}$$

where m is the number of points in the neighborhood of ζ, U_I, V_I and W_I are the components of the displacement vector of the Ith point in the $\mathbf{E}_1$, $\mathbf{E}_2$ and $\mathbf{E}_3$ directions, respectively. The vectors $\mathbf{U}$, $\mathbf{T}$ and $\Delta\mathbf{T}$ are defined as

$$\mathbf{U} = (U\ \ V\ \ W)^{\mathrm{T}}, \quad \mathbf{T} = (T_1\ \ T_2)^{\mathrm{T}} \quad \text{and} \quad \Delta\mathbf{T} = (\Delta T_1\ \ \Delta T_2)^{\mathrm{T}}.$$

Using Eqs. (17), (20) and (22), the static variation form (23) can be written as

$$W_{\mathrm{Sta}}(\delta\mathbf{x}) = \int_{\mathbb{A}} \left[[\mathbf{H}_{mm}\delta\mathbf{U}]^{\mathrm{T}}\tilde{\mathbf{n}} + [\mathbf{H}_{bm}\delta\mathbf{U} + \mathbf{H}_{bb}\delta\mathbf{T}]^{\mathrm{T}}\tilde{\mathbf{m}} + [\mathbf{H}_{sm}\delta\mathbf{U} + \mathbf{H}_{sb}\delta\mathbf{T}]^{\mathrm{T}}\tilde{\mathbf{q}}\right] \mathrm{d}\mathrm{Re} - W_{\mathrm{ext}}(\delta\mathbf{U}, \delta\mathbf{T}). \tag{33}$$

Here, the respective matrices are defined as

$$\mathbf{H}_{mm} = \begin{bmatrix} \boldsymbol{\varphi}_{,1}\frac{\partial}{\partial\xi^1} \\ \boldsymbol{\varphi}_{,2}\frac{\partial}{\partial\xi^2} \\ \boldsymbol{\varphi}_{,1}\frac{\partial}{\partial\xi^2} + \boldsymbol{\varphi}_{,2}\frac{\partial}{\partial\xi^1} \end{bmatrix}_{3\times 3},$$

$$\mathbf{H}_{sm} = \begin{bmatrix} \mathbf{t}\frac{\partial}{\partial\xi^\alpha} \\ \mathbf{t}\frac{\partial}{\partial\xi^\beta} \end{bmatrix}_{2\times 3}, \quad \mathbf{H}_{sb} = \begin{bmatrix} \boldsymbol{\varphi}_{,1} \\ \boldsymbol{\varphi}_{,2} \end{bmatrix}_{2\times 3} \overline{\boldsymbol{\Psi}}_{3\times 2},$$

$$\mathbf{H}_{bm} = \begin{bmatrix} \mathbf{t}_{,1}\frac{\partial}{\partial\xi^1} \\ \mathbf{t}_{,2}\frac{\partial}{\partial\xi^2} \\ \mathbf{t}_{,1}\frac{\partial}{\partial\xi^2} + \mathbf{t}_{,2}\frac{\partial}{\partial\xi^1} \end{bmatrix}_{3\times 3} \quad \text{and} \quad \mathbf{H}_{bb} = \begin{bmatrix} \boldsymbol{\varphi}_{,1}\frac{\partial}{\partial\xi^1} \\ \boldsymbol{\varphi}_{,2}\frac{\partial}{\partial\xi^2} \\ \boldsymbol{\varphi}_{,1}\frac{\partial}{\partial\xi^2} + \boldsymbol{\varphi}_{,2}\frac{\partial}{\partial\xi^1} \end{bmatrix}_{3\times 3} \overline{\boldsymbol{\Psi}}_{3\times 2}. \tag{34}$$

The important feature of the resultant shell theory is that the interpolations of the reference director field $\mathbf{t}$ and the linearized field $\Delta\mathbf{t}$ have to be computed. Let $\mathbf{t}_I$ denote the directors at the EFG nodal points. The interpolation of the reference director field $\mathbf{t}$ can be expressed as

$$\mathbf{t} = \frac{\sum_{I=1}^{m}\phi_I\mathbf{t}_I}{\left\|\sum_{I=1}^{m}\phi_I\mathbf{t}_I\right\|} = \frac{\tilde{\mathbf{t}}}{\|\tilde{\mathbf{t}}\|}, \tag{35}$$

where m is the number of nodes in the neighborhood. The interpolation of the linearized field $\Delta\mathbf{t}$ is consistent with the expression of the reference director field $\mathbf{t}$ and is given by

$$\Delta\mathbf{t} = \sum_{I=1}^{m}\frac{(1-\mathbf{t}\otimes\mathbf{t})}{\|\tilde{\mathbf{t}}\|}\phi_I\Delta\mathbf{t}_I. \tag{36}$$

The derivatives of the director field $\mathbf{t}_{,\alpha}$ and linearized field $\Delta\mathbf{t}_{,\alpha}$ must be calculated to obtain the interpolation for bending strain measures. The derivatives of the director field $\mathbf{t}_{,\alpha}$ can be expressed as

$$\mathbf{t}_{,\alpha} = \frac{1}{\|\tilde{\mathbf{t}}\|}\left(\tilde{\mathbf{t}}_{,\alpha} - \mathbf{t}\left(\mathbf{t}\cdot\tilde{\mathbf{t}}_{,\alpha}\right)\right). \tag{37}$$

Hence, the derivatives of linearized field $\Delta\mathbf{t}_{,\alpha}$ can be written as

$$\Delta\mathbf{t}_{,\alpha} = \sum_{I=1}^{m}\frac{1}{\|\tilde{\mathbf{t}}\|}\left\{(\mathbf{1}-\mathbf{t}\otimes\mathbf{t})\phi_{I,\alpha} - \left[\mathbf{t}_{,\alpha}\otimes\mathbf{t} + \mathbf{t}\otimes\mathbf{t}_{,\alpha} + \frac{1}{\|\tilde{\mathbf{t}}\|}\left(\mathbf{t}\cdot\tilde{\mathbf{t}}_{,\alpha}\right)(\mathbf{1}-\mathbf{t}\otimes\mathbf{t})\right]\phi_I\right\}\Delta\mathbf{t}_I, \tag{38}$$

where $\tilde{\mathbf{t}}_{,\alpha}$ is given by

$$\tilde{\mathbf{t}}_{,\alpha} = \sum_{I=1}^{m}\phi_{I,\alpha}\mathbf{t}_I. \tag{39}$$

Substituting the displacement field of forms (31) and (32) into the variational form (32), the finial static discrete equation of penalty method can be obtained as

$$\left(\mathbf{K}+\tilde{\mathbf{K}}\right)\overline{\mathbf{U}} = \overline{\mathbf{F}}, \tag{40}$$

where $\mathbf{K}$ is the global stiffness and matrix. The contribution of the membrane stress, bending stress resultant and shear stress resultant to the stiffness matrix associated with nodes (I, J) are denoted by $\mathbf{K}_{IJ}^m$, $\mathbf{K}_{IJ}^b$ and $\mathbf{K}_{IJ}^s$,

which are given by

$$\mathbf{K}_{IJ}^{m} = \int_{\mathrm{Re}} \mathbf{H}_{mm(I)}^{\mathrm{T}} \mathbf{D}_1 \mathbf{H}_{mm(J)} \, \mathrm{dRe} \tag{41}$$

$$\mathbf{K}_{IJ}^{b} = \int_{\mathrm{Re}} \begin{pmatrix} \mathbf{H}_{bm(I)}^{\mathrm{T}} \\ \mathbf{H}_{bb(I)}^{\mathrm{T}} \end{pmatrix} \mathbf{D}_2 (\mathbf{H}_{bm(J)} \;\; \mathbf{H}_{bb(J)}) \, \mathrm{dRe}, \tag{42}$$

$$\mathbf{K}_{IJ}^{s} = \int_{\mathrm{Re}} \begin{pmatrix} \mathbf{H}_{sm(I)}^{\mathrm{T}} \\ \mathbf{H}_{sb(I)}^{\mathrm{T}} \end{pmatrix} \mathbf{D}_3 (\mathbf{H}_{sm(J)} \;\; \mathbf{H}_{sb(J)}) \, \mathrm{dRe} \tag{43}$$

$$\tilde{\mathbf{K}}_{IJ} = \int_{\mathrm{Re}_u} \mathbf{\Phi}_I^{\mathrm{T}} \boldsymbol{\alpha} \mathbf{\Phi}_J \, \mathrm{dRe}, \tag{44}$$

$$\overline{\mathbf{F}}_I = \int_{\mathbb{A}} (\mathbf{\Phi}_I^{\mathrm{T}} \overline{\mathbf{n}} + (\bar{j})^{-1} \mathbf{\Phi}_I^{\mathrm{T}} \overline{\tilde{\mathbf{m}}}) \, \mathrm{dRe} + \int_{\partial_n \mathbb{A}} \bar{j} \mathbf{\Phi}_I^{\mathrm{T}} \overline{\mathbf{n}} \, \mathrm{ds} + \int_{\partial_m \mathbb{A}} \mathbf{\Phi}_I^{\mathrm{T}} \overline{\mathbf{m}} \, \mathrm{d}s + \int_{\mathbb{A}} \mathbf{\Phi}_I^{\mathrm{T}} \boldsymbol{\alpha} \overline{\mathbf{u}}_I \, \mathrm{dRe}, \tag{45}$$

where $\mathbf{U}$ is a vector of generalized displacement and is written as

$$\overline{\mathbf{U}} = (U \;\; V \;\; W \;\; \Delta T_1 \;\; \Delta T_2)^{\mathrm{T}}. \tag{46}$$

For eigenvalue analysis, the essential boundary conditions are homogeneous. The displacement can be expressed as

$$\overline{\mathbf{U}} = \tilde{\mathbf{U}} \mathrm{e}^{\mathrm{i}\omega \mathrm{t}}, \tag{47}$$

where i is the imaginary unit, ω is the angular frequency and U is the amplitude of the vibration.

Substituting the displacement field of forms (31) and (32) into the variational form for free vibration (26), the discrete equation of penalty method for dynamic analysis can be obtained as

$$\mathbf{M}\ddot{\mathbf{U}} + (\mathbf{K} + \tilde{\mathbf{K}})\overline{\mathbf{U}} = 0, \tag{48}$$

The eigenvalue equations of the shells derived from Eq. (48) is of the form

$$[(\mathbf{K} + \tilde{\mathbf{K}}) - \omega^2 \mathbf{M}]\tilde{\mathbf{U}} = 0, \tag{49}$$

Where $\tilde{\mathbf{U}}$ is an egenvector in the form of

$$\tilde{\mathbf{U}} = \{U_1 \;\; U_2 \;\; U_3 \ldots U_n\}^{\mathrm{T}}.$$

As the penalty technique is used to impose the essential boundary conditions, an additional matrix is introduced into Eq. (49), the eigenvalue equation can be conveniently calculated using standard routines.

In order to obtain the integrals defined by Eqs. (41)–(45), a background cell structure is needed, which maybe independent of the scattered nodes for interpolation. In each background cell, Gauss quadrature is employed. The number of Gauss points is determined by the accuracy requirements. A detailed investigation is given by Krysl and Belytschko [21] on the relation between density of nodes and density of Gauss points. A quadrature at 6×6 integration stations are adopted in the paper. It is also noted that the mass matrix is in consistent form and is adopted in the following numerical examples.

3. Numerical examples

The present method is tested on several common benchmark problems. Numerical integration with 6×6 Gaussian quadrature on the background elements is used in all numerical examples. The essential boundary conditions are enforced by the penalty method. The linear shape functions with one-point quadrature in enforcing the essential boundary conditions are used in all numerical examples describe in the paper.

3.1. Static problems for shells

3.1.1. Barrel vault roof

The performance of the present method is evaluated on a standard test problem of a barrel vault roof shown in Fig. 2. The shell roof is loaded by its own uniform vertical gravity load. It is supported by diaphragms along the curved ends, but is free along the straight edges. The following parameters are used: length $L = 600$, radius $R = 300$, thickness $h = 3.0$ and the semi-span-angle of the section is $\theta = 40^\circ$. The Young's modulus is $E = 3.0 \times 10^6$; the Poisson's ratio is $v = 0$ and the mass density is $\rho = 0.20833$.

This problem is commonly used for determining the ability of the shell formulations to accurately solve complex states of membrane strain. A substantial part of the strain energy is membrane strain energy and the representation of inextensional modes is not crucial in this problem [22]. Therefore inadequacies in membrane stress analysis will severely inhibit convergence. Using symmetry, only one-quarter of panel needs to be modeled. There is a convergent solution of magnitude -3.618 for the vertical deflection at point A, which is used to normalize the result in Fig. 3. The polynomial bases adopted for this problem are quadratic and quartic for standard EFG and quadratic for the MEFG. The convergence of the present analysis is excellent in comparison with the results of high-performance FEM by Simo et al. [20], by the EFG method for thin shells [16], by the EFG method for general shell [18]. It can be seen that the convergence rate of quartic basis always exceeds that of quadratic basis for EFG. The result for quartic basis approaches the exact result from above with increase in numbers of EFG nodes, while that for quadratic basis oscillates along the exact result with increase in EFG nodes. It should be mentioned that there are only 3 dof assigned to each point for the Kirchhoff–Love model of thin shells by Krysl and Belytschko [16]. It also should be noted that the result and the convergence rate of quadratic basis for MEFG are better than that of quadratic basis for standard EFG. The reason is that MEFG shows a complete absence of shear locking which can give a correct estimation of shear energy.

Fig. 4 shows the variation of shear, membrane and bending energies with respect to the size of domain of influence using quartic basis. It can be seen that membrane and bending energies remain constant regardless of domain size; the difference between the membrane and bending energies are no more than 4.0%. The shear energy is very small and approaches zero with increase in EFG nodes, which means the shear stress plays almost no role in the displacement response of this problem.

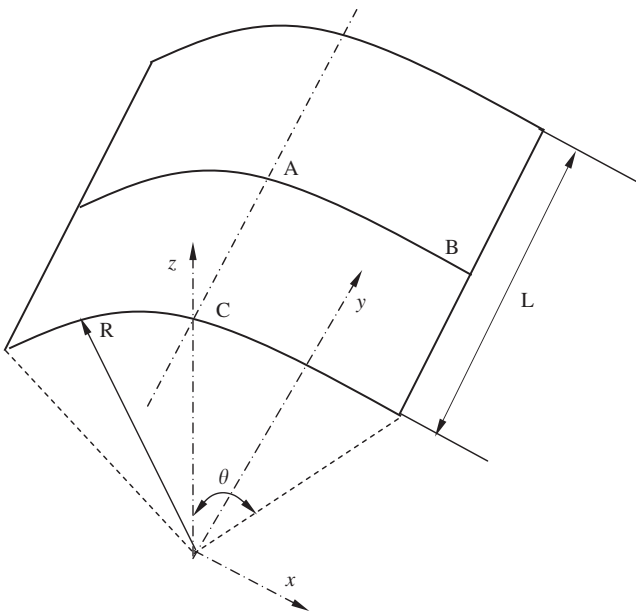

Fig. 2. Barrel vault roof.

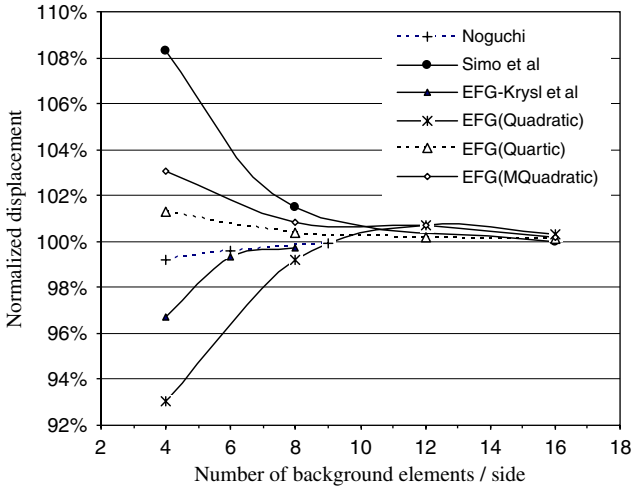

Fig. 3. Convergence of vertical displacement.

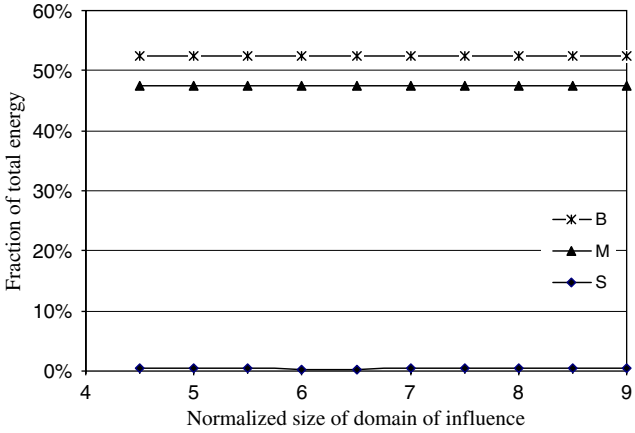

Fig. 4. Convergence of membrane (M), shear (S) and bending (B) energies with size of domain of influence.

The comparison of computational efficiency of the EFGM for spatial shells with respect to the FEM is discussed. The model consists of 8×8 integration background meshes, with the scattered nodes located at the vertices of the cells. Numerical integration is carried out on the background elements using a 6×6 Gaussian quadrature. The computations are carried out on the slave nodes of Linux Beowulf Cluster (IBM xSeries 330 with 1G hz PIII CPU/256MB L2 cache, 18 GB SCSI HDD and 1GB RAM). Figs. 5 and 6 show the variation of displacement of the point A and the variation of computation time with the size of influence domain for EFG method, respectively. The minimum distance between nodes is utilized to normalize the size of domain of influence. Solving the problem using the same number of nodes by FEM commercial software, such as ANSYS, requires a computation time of about 13 s and the error between the convergent numerical results and the numerical results is greater than 1.5%. The EFG method can be found to be 10 to 50 times slower than the FEM for this problem in order to get an acceptable result. The major disadvantage of EFG method is that the construction of EFG shape function is computationally more expensive. For the EFG method, the number of the nodes is usually greater than the number of monomials in the polynomial basis in order to obtain an accurate shape function, especially for the analysis of shell structures. In general, it takes extra effort to choose and compute the weight functions. The reason is that the weight functions play an important role in the performance of the EFG method and are usually different for different problems. It also should be noted that the nodal parameters are not the nodal values, which means that the approximation of the value at a certain

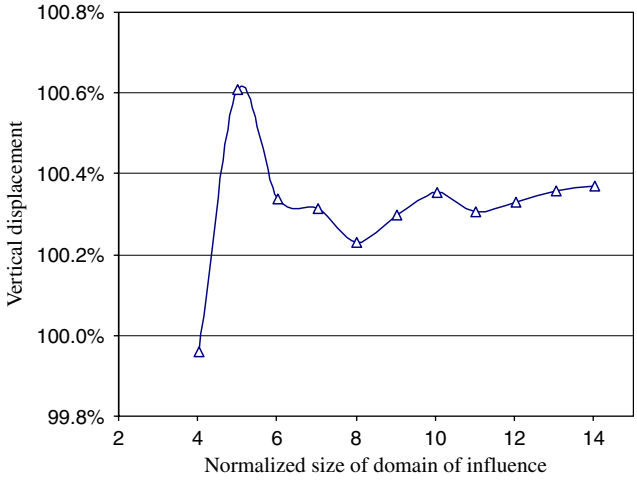

Fig. 5. Variation of displacement of point B with size of influence domain.

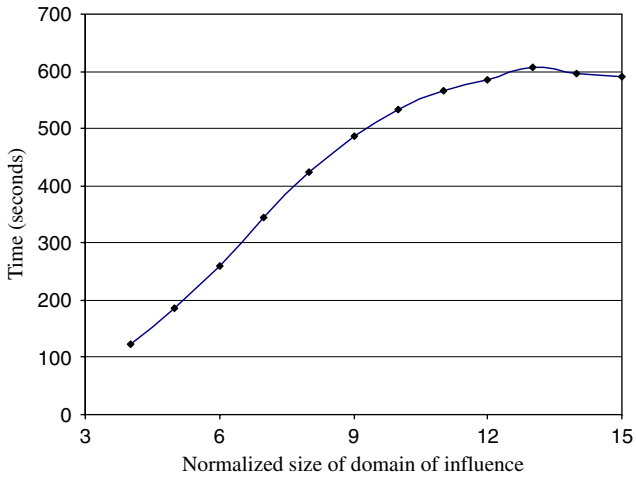

Fig. 6. Variation of computation time with size of influence domain.

node depends on the nodal parameter of this node as well as the nodal parameters of the nodes in its influence domain.

3.1.2. Pinched cylindrical shell

The second test problem involves a thin cylindrical shell loaded by two centrally located and diametrically opposing concentrated forces as shown in Fig. 7. The ends of the cylinder are supported by rigid diaphragms which allow displacement in the axial direction and rotation about the tangent to the shell boundary. The length of the cylinder is $L = 600$, the radius is $R = 300$, and the thickness is $h = 3$. The material properties are $E = 3.0 \times 10^6$ and $v = 0.3$.

This problem is one of the most severe tests for both inextensional bending and complex membrane states of stress. Using symmetry, only one-eighth of the cylinder needs to be modeled by present method. There is a convergent numerical solution of 1.8248e-5 for the radial displacement at the loaded points, which was used to normalize the results in Fig. 8. The convergence by the present method is excellent in comparison with the results from FEM [20], the EFG method for thin shells [16] and the common commercial software ABAQUS using S4R elements. S4R element means the 4-node doubly curved general-purpose shell element and reduced integration with hourglass control is used.

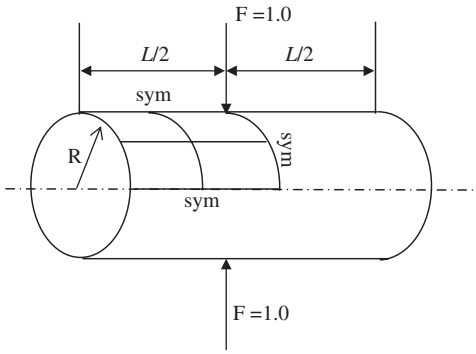

Fig. 7. Pinched cylindrical shell.

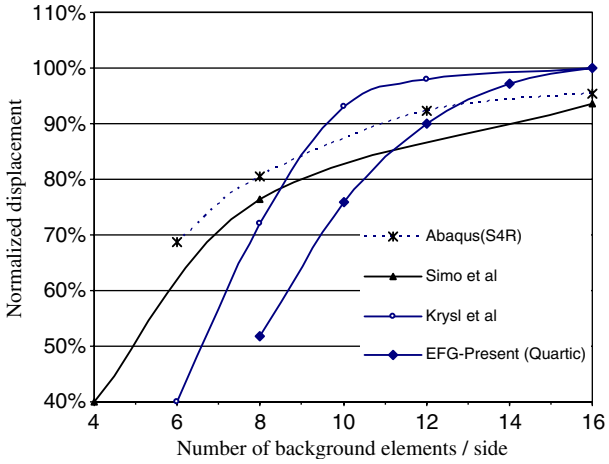

Fig. 8. Convergence of central displacement.

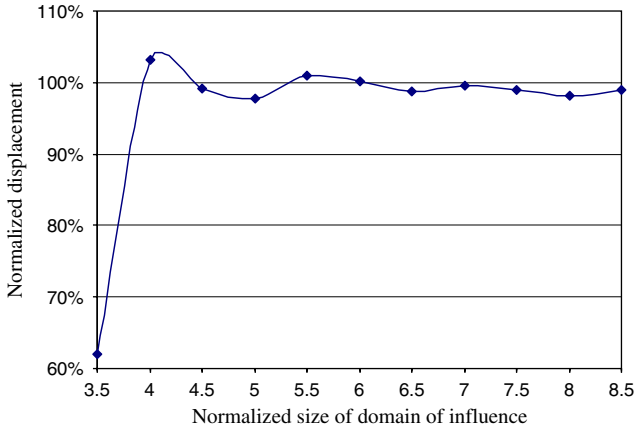

Fig. 9. Variation of displacement with size of domain of influence.

The variation of displacement at the central point with the size of domain of influence is shown in Fig. 9. The minimum distance between nodes is utilized to normalize the size of domain of influence. The fluctuation of the normalized displacement is less than 2.8% when the support domain is large. The fractions of total energy as membrane, shear and bending energies are shown in Fig. 10. The membrane energy is over predicted

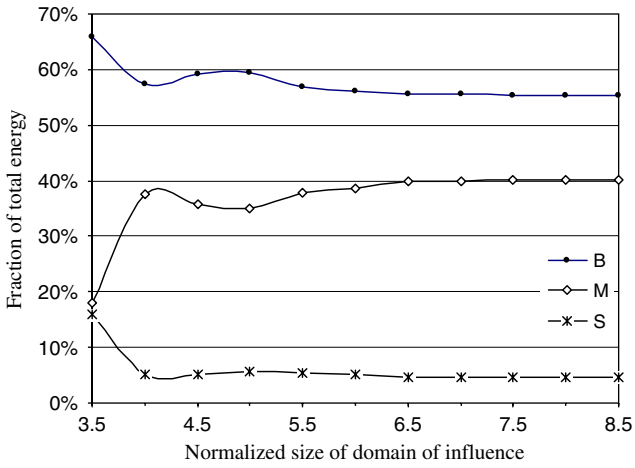

Fig. 10. Convergence of membrane (M), shear (S) and bending (B) energies with size of domain of influence.

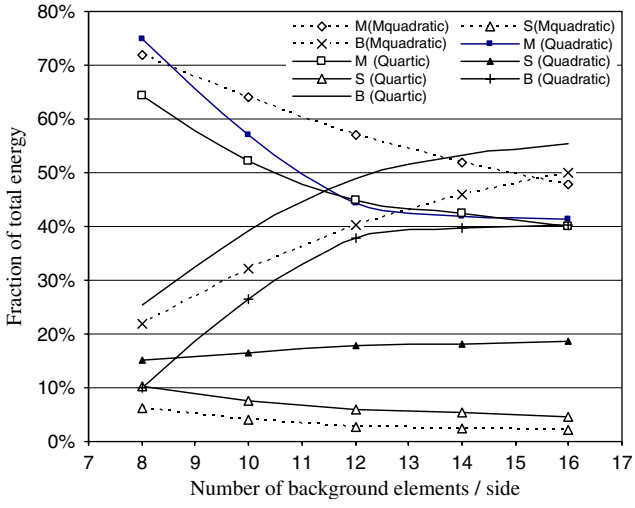

Fig. 11. Convergence of membrane, shear and bending energies.

for the coarse arrangement nodes, which is indicative of membrane locking. All energies show the similar fluctuating trends as that observed for displacement. For domain size between 5.5 and 8.5, the displacement and energies are relatively constant. It is also interested to see that membrane energy fraction increases initially and accompanies by the decrease of the shear energy fraction. Maybe the reason is that the initial addition of scatter nodes serves primarily to reduce the shear locking and the total internal energy is very small because of severe locking.

Fig. 11 shows the fractions of total energy, as shear, membrane and bending energies for both quartic and quadratic polynomial bases of standard EFG and quadratic polynomial base of MEFG (modified EFG). As can be seen, for quartic polynomial basis, the shear energy fraction tends to be less than 4.0% as the number of EFG nodes increase, which means that shear stress plays a minor role in the displacement response. The membrane energy fraction is approximately 40.0%, which agrees satisfactorily with the results from the 9-noded Gamma FEM by Belytschko et al. [9]. For the quadratic polynomial basis, the membrane fraction tends to be 40.0%, similar to that for the quartic polynomial basis, however, the shear energy increases with the addition of EFG nodes and play an important role in the problem. It can be seen that for sparse discrete nodes, membrane locking is dominant, while for the dense nodes, shear locking becomes more important. For

quadratic basis of MEFG, it can be seen that the shear energy fraction tends to almost zero with the increase of scatter nodes and even less than that of quartic basis of standard EFG, which means using high order basis function may alleviate but not totally suppress shear locking effects. The good results cannot be obtained by the quadratic basis of MEFG because membrane energy is over predicted even a lot of scatter nodes are used in the problem, which is indicative of membrane locking occurs primarily in curved structures. Kanok-Nukulchai [11] demonstrated that MEFG method could completely eliminated the presence of transverse shear locking when the matching fields concept is employed. However the results given here shows that the MEFG method could not work efficiently for the shell problems occurring shear locking and membrane locking.

3.2. Frequency analysis for shells

The performance characteristics of the EFG method for the free vibration analysis are also evaluated. The results of several examples are presented and compared with analytical solution and other results to show their accuracy and validity.

3.2.1. Free vibration of a clamped cylindrical shell panel

The free vibration test performed by Petyt [23] on a clamped shallow shell panel provides a good reference for comparison. The geometry and boundary conditions of the shell panel are shown in Fig. 12 and the following parameters are used in the analysis: length $L = 76.2\,\text{mm}$, radius $R = 762\,\text{mm}$, thickness $h = 0.33\,\text{mm}$. The Young's modulus is $E = 6.8948 \times 10^{10}\,\text{N/m}^2$; the Poisson's ratio is $v = 0.33$ and the mass density is $\rho = 2657.3\,\text{kg/m}^3$. The central subtended angle of the section is $\theta = 7.64^\circ$.

Petyt [23] carried out a comparison between the experimental natural frequencies and those obtained by four different numerical method, namely extended Raleigh–Ritz method (ERR), triangular finite element method (FET) and rectangular finite element method (FER) and Kantorovich. Regular nodes of different densities are used to investigate the convergence characteristics of natural frequencies and the results are given in Table 1. The values of natural frequency of the shell panel are also presented in Table 2 together with experimental results and results obtained by Petyt [23] and isoparametric spline finite strip method. It can be seen that the EFG results show good convergence and good agreement with other methods.

3.2.2. Free vibration of a clamped–free hyperboloidal shell

Hyperboloidal shells are of considerable practical importance, because of their frequent use as reinforced concrete hyperbolic cooling towers. This particular problem has been shown to be particularly difficult

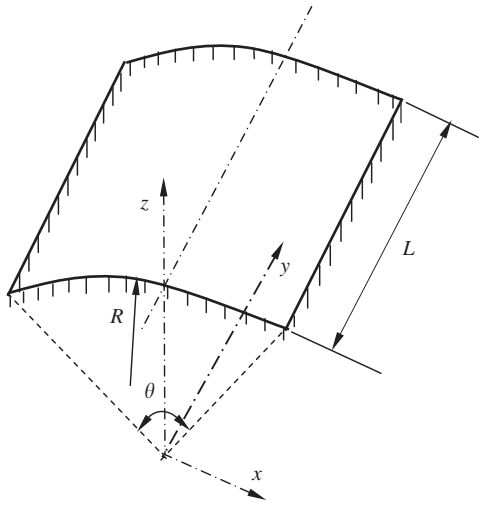

Fig. 12. Clamped cylindrical shell panel.

Table 1
Natural frequencies of a clamped cylinder panels (Hz). Results of convergence study

Mode	MEFG (Quadratic)			
	7×7	9×9	13×13	17×17
1	827.8	861.2	869.1	870.8
2	923.0	960.7	959.0	961.4
3	1193.7	1297.2	1294.1	1295.6
4	1361.7	1385.6	1369.4	1368.9
5	1454.4	1435.7	1446.1	1440.7
6	1600.7	1729.2	1751.7	1749.2
7	1730.4	1761.5	1775.3	1780.5
8	1934.2	2055.5	2062.0	2056.9
9	2133.1	2209.4	2224.4	2227.3
10	2238.3	2290.4	2277.2	2293.6

Table 2
Natural frequencies of clamped cylinder panels. Comparison of experimental and numerical results

Mode	Experimental results	ERR	FET	FER	K	Present method (17×17)
1	814	870	970	890	890	870.8
2	940	958	958	973	966	961.4
3	1260	1288	1288	1311	1295	1295.6
4	1306	1364	1363	1371	1375	1368.9
5	1452	1440	1440	1454	1450	1440.7
6	1802	1753	1756	1775	1745	1749.2
7	1735/1770	1795	1780	1816		1780.5
8	2100	2057	2056	2068		2056.9
9	2225	2220	2222	2234		2227.3
10	2280	2300	2295	2319		2293.6

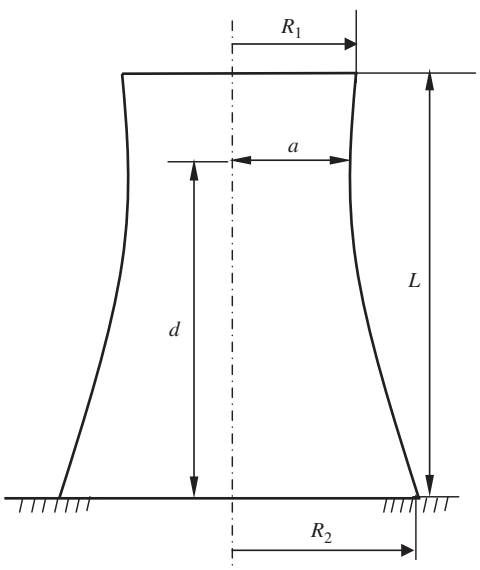

Fig. 13. Geometry of clamped–free hyperboloidal shell.

Table 3
Natural frequency (Hz) of a clamped–free hyperboloidal shell

Mode	Özakca and Hinton [24]	Carter et al. [25]	Present method (EFG) Quartic	
			13×17	19×25
			(axial × circum)	
1	1.0354	1.0348	1.0307	1.0312
2	1.1508	1.1467	1.1412	1.1436
3	1.1826	1.1808	1.1698	1.1743
4	1.3061	1.3015	1.2901	1.2972
5	1.3293	1.3231	1.3127	1.3179
6	1.3758	1.3749	1.3665	1.3711
7	1.4329	1.4293	1.4188	1.4224
8	1.4488	1.4475	1.4393	1.4423

because slight variation in geometry leads to large chances in the natural frequencies. The geometry of a clamped–free hyperboloidal shell is shown in Fig. 13. The shell geometry is defined by the equation of its meridian

$$\left(\frac{R}{a}\right)^2 - \left(\frac{L-d}{b}\right)^2 = 1, \tag{50}$$

where b is a characteristic dimension of the shell defined as $b = ad/\sqrt{R_2^2 - a^2}$. The following geometric and material properties are used in the analysis: $L = 100.787\,\text{m}$, $h = 0.127\,\text{m}$, $a = 25.603\,\text{m}$, $b = 63.906\,\text{m}$, $d = 82.194\,\text{m}$, Young's modulus $E = 2.069 \times 10^{10}\,\text{N/m}^2$, Poisson's ratio $v = 0.15$, and the mass density $\rho = 2405\,\text{kg/m}^3$. A regular nodal arrangement in the axial and circumferential direction is used in the analysis. The results of the present study using different number of nodes are given in Table 3 together with those obtained by Özakca and Hinton [24] using the FEM and Carter et al. [25] using a numerical integration technique based on classical thin shell theory. Close agreement can again be observed in Table 3.

4. Conclusion

The EFG method has been utilized to analyze spatial shell structures based on the stress resultant shell geometrically exact theory, which has only 5 dof assigned to every point of the shell. The 3-D classical continuum of a shell is modeled directly as a 2-D Cosserat surface thus avoiding any explicit kinematical assumptions. By using the background stretch method, the geometry of an arbitrary curved surface is mapped to a 2-D space and each discrete EFG node has a unique parameter value.

For thick shells, the formulation allows for transverse shear strain and results in the Mindlin plate when the surface is flat and membrane state is negligible. In order to avoid shear locking and membrane locking, a quartic basis function is adopted for the MLS approximation. Using high-order basis functions alleviate shear locking. This method is easily implemented for the EFG method because MLS shape functions are obtained from the discrete EFG nodes. Therefore, the formulation is available for both thin and thick shells. Several benchmark shell examples are analyzed to show the validity of the proposed method and satisfied results obtained are in good agreement with theoretical and FE results. However, it should be noted that recourse must be taken to meshes for the integration of the weak form of governing equations by the EFG method presented in the paper.

Appendix A. MLS approximation

In the paper, the MLS approximation method is used to approximate the displacement and the surface geometry of the shell. The derivations of shape functions from the MLS approximation method were presented by Nayroles et al. [26] and Belytschko et al. [27]. A 2-D field is assumed for modeling thin shell and

membrane structures. A component of the displacement vector is approximated by a polynomial function as follows

$$u^h(\mathbf{x}) = \mathbf{P}^{\mathrm{T}}(\mathbf{x})\mathbf{a}(\mathbf{x}), \tag{A.1}$$

where $\mathbf{P}(\mathbf{x})$ is the polynomial function and $\mathbf{a}(\mathbf{x})$ is the vector of coefficients. The complete polynomial basis of n terms of order s in two dimensions is given by (see Ref. [27])

$$\mathbf{P}^{\mathrm{T}}(\mathbf{x}) = \mathbf{P}^{\mathrm{T}}(x, y) = \left\{1, x, y, x^2, xy, y^2, \ldots, x^s, \ldots xy^{s-1}, y^s\right\}^{\mathrm{T}}. \tag{A.2}$$

The unknown coefficients $\mathbf{a}(\mathbf{x})$ are solved by minimizing the following weighted residual

$$J = \sum_{I=1}^{m} w(\mathbf{x} - \mathbf{x}_I)\left[\mathbf{P}^{\mathrm{T}}(\mathbf{x})\mathbf{a}(\mathbf{x}) - u_I\right]^2, \tag{A.3}$$

where $w(\mathbf{x}-\mathbf{x}_I)$ is the weight function of compact support (often called the domain of influence of node I), m is the number of points in the neighborhood of $\mathbf{x}$, u_I is an unknown nodal value of $\mathbf{u}$ at a sampling point $\mathbf{x}_I$.

The stationary condition of J in Eq. (A.3) with respect to $\mathbf{a}(\mathbf{x})$ yields the following linear system of equations

$$\mathbf{A}(\mathbf{x})\mathbf{a}(\mathbf{x}) = \mathbf{B}(\mathbf{x})\mathbf{u}, \tag{A.4}$$

where $\mathbf{u}$ consists of the nodal values u_I. The symmetrical matrix $\mathbf{A}(\mathbf{x})$ and the non-symmetrical matrix $\mathbf{B}(\mathbf{x})$ are defined as

$$\mathbf{A}(\mathbf{x}) = \sum_{I=1}^{m} w(\mathbf{x} - \mathbf{x}_I)\mathbf{P}(\mathbf{x}_I)\mathbf{P}^{\mathrm{T}}(\mathbf{x}_I),$$

$$\mathbf{B}(\mathbf{x}) = [w(\mathbf{x} - \mathbf{x}_1)\mathbf{P}(\mathbf{x}_1), \ldots, w(\mathbf{x} - \mathbf{x}_m)\mathbf{P}(\mathbf{x}_m)]. \tag{A.5}$$

Substituting Eq. (A.5) into Eq. (A.1) yields

$$u^h(\mathbf{x}) = \mathbf{P}^{\mathrm{T}}(\mathbf{x})\mathbf{A}^{-1}(\mathbf{x})\mathbf{B}(\mathbf{x})\mathbf{u} = \mathbf{\Phi}^{\mathrm{T}}(\mathbf{x})\mathbf{u} = \sum_{I=1}^{m} \phi_I(\mathbf{x})u_I, \tag{A.6}$$

where the shape function $\phi_I(\mathbf{x})$ is a component of vector $\mathbf{\Phi}^{\mathrm{T}}(\mathbf{u})$. It can also be written as

$$\phi_I(\mathbf{x}) = \mathbf{P}^{\mathrm{T}}(\mathbf{x})\mathbf{A}^{-1}(\mathbf{x})\mathbf{B}_I(\mathbf{x}) = \boldsymbol{\gamma}^{\mathrm{T}}(\mathbf{x})\mathbf{B}_I(\mathbf{x}), \tag{A.7}$$

where $\boldsymbol{\gamma}^{\mathrm{T}}(\mathbf{x}) = \mathbf{P}^{\mathrm{T}}(\mathbf{x})\mathbf{A}^{-1}(\mathbf{x})$. This leads to the relationship

$$\mathbf{A}(\mathbf{x})\boldsymbol{\gamma}(\mathbf{x}) = \mathbf{P}(\mathbf{x}). \tag{A.8}$$

The weight function $w(\mathbf{x} - \mathbf{x}_I)$ plays an important role in the performance of the EFG method. A poorly constructed weight function will not guarantee a unique solution of $\mathbf{a}(\mathbf{x})$. The weight functions are positive and decrease in magnitude as the distance from $\mathbf{x}$ to $\mathbf{x}_I$ increases.

In this paper, the quartic spline weight function is chosen on account of the requirements on the continuity of the function and its derivatives. The spline is expressed as a function of normalized distance [27]

$$w(r) = \begin{cases} \left(1 - 6r^2 + 8r^3 - 3r^4\right) & \text{for } 0 \leqslant r \leqslant 1, \\ 0 & \text{for } > 1 \end{cases} \tag{A.9}$$

with the normalized distance r being $r = \rho/R_I$, where R_I is the radius of the support of the Ith node. The choice of the shape of the domain is arbitrary, but square domains and the circular domains are the most common. In this paper, circular domains are used. Therefore, weight functions depend only on the distance between two points as follows

$$w(\mathbf{x} - \mathbf{x}_I) = w_I(\rho), \tag{A.10}$$

where $\rho = \|\mathbf{x} - \mathbf{x}_I\|$ is the distance between the two points $\mathbf{x}$ and $\mathbf{x}_I$. The support radius can be computed from the arrangement of the EFG points by defining the domain of each quadrature point to include the required number of EFG points for evaluating the partial derivatives of the shape function.

In the paper, the two different polynomial basis adopted are (i) quadratic and (ii) quartic to ameliorate shear and membrane locking [16]

$$\text{(i)}\ \ \mathbf{P}^{\mathrm{T}}(\mathbf{x}) = \left\{1, x, y, x^2, xy, y^2\right\}, \quad (n = 6), \tag{A.11}$$

$$\text{(ii)}\ \ \mathbf{P}^{\mathrm{T}}(\mathbf{x}) = \left\{1, x, y, x^2, xy, y^2, x^3, x^2y, xy^2, y^3, x^4, x^3y, x^2y^2, xy^3, y^4\right\}^{\mathrm{T}} \quad (n = 15). \tag{A.12}$$

References

[1] H.T.Y. Yang, S. Saigal, D.G. Liaw, A survey of recent shell finite elements, *International Journal for Numerical Methods in Engineering* 47 (2000) 101–127.

[2] D. Chapelle, K.J. Bathe, Fundamental considerations for the finite element analysis of shell structures, *Computers and Structures* 66 (1998) 19–36.

[3] C. Baiocchi, C. Lovadina, A shell classification by interpolation, *Mathematical Models and Methods in Applied Science* 12 (2002) 1359–1380.

[4] D. Chapelle, K.J. Bathe, *The Finite Element Analysis of Shells—Fundamentals*, Springer, Berlin, 2003.

[5] F. Auricchio, L. Beirãoda Veiga, C. Lovadina, Remarks on the asymptotic behavior of Koiter shells, *Computers and Structures* 80 (2002) 735–745.

[6] E. Carrera, Theories and finite elements for multilayered anisotropic, composite plates and shells, *Archives of Computational Methods in Engineering* 9 (2002) 87–140.

[7] E. Carrera, Theories and finite elements for multilayered plates and shells: a unified compact formulation with numerical assessment and benchmarking, *Archives of Computational Methods in Engineering* 10 (2003) 215–297.

[8] J.L. Eriksen, C. Truesdell, Exact theory of stress and strain in rod and shells, *Archive for Rational Mechanics and Analysis* 1 (1958) 295–323.

[9] J. Simo, D.D. Fox, On a stress resultant geometrically exact shell model—part I: formulation and optimal parameterization, *Computer Methods in Applied Mechanics and Engineering* 72 (1989) 267–304.

[10] B.M. Donning, W.K. Liu, Meshless methods for shear-deformable beams and plates, *Computer Methods in Applied Mechanics and Engineering* 152 (1998) 47–72.

[11] W. Kanok-Nukulchai, W. Barry, K. Saran-Yasoontorn, P.H. Bouillard, On elimination of shear locking in the element-free Galerkin method, *International Journal for Numerical Methods in Engineering* 52 (2001) 705–725.

[12] J. Piila, Y. Leino, O. Ovaskainen, J. Pitkäranta, Shell deformation states and the finite element method: a benchmark study of cylindrical shells, *Computer Methods in Applied Mechanics and Engineering* 128 (1995) 81–121.

[13] K.J. Bathe, P.S. Lee, D. Chapelle, A shell problem highly sensitive to thickness changes, *International Journal for Numerical Methods in Engineering* 57 (2003) 1039–1052.

[14] L. Beirão da Veiga, Uniform error estimates for a class of intermediate cylindrical shell problems, *Numerische Mathematik* 96 (2004) 661–689.

[15] L. Beirão da Veiga, Asymptotic study of the solution for pinched cylindrical shells, *Computer Methods in Applied Mechanics Engineering* 194 (2005) 1113–1139.

[16] P. Krysl, T. Belytschko, Analysis of thin shells by element-free Galerkin method, *International Journal of Solids and Structures* 33 (1996) 3057–3080.

[17] S. Li, W. Hao, W.K. Liu, Numerical simulations of large deformation of thin shell structures using meshfree methods, *Computational Mechanics* 25 (2000) 102–116.

[18] H. Noguchi, T. Kawashima, T. Miyamura, Element free analyses of shell and spatial structures, *International Journal for Numerical Methods in Engineering* 47 (1997) 1215–1240.

[19] L. Liu, G.R. Liu, V.B.C. Tan, Element free method for static and free vibration analysis of spatial thin shell structures, *Computer methods in Applied Mechanics and Engineering* 191 (2002) 5923–5942.

[20] J. Simo, D.D. Fox, M.S. Rifai, On a stress resultant geometrically exact shell model—part II: the linear theory, *Computer Methods in Applied Mechanics and Engineering* 73 (1989) 53–92.

[21] P. Krysl, T. Belytschko, Analysis of thin plates by element-free Galerkin method, *Computational Mechanics* 17 (1995) 26–35.

[22] T. Belytschko, H. Stolarski, W.K. Liu, N. Carpenter, J.S.-J. Ong, Stress projection for membrane and shear locking in shell finite elements, *Computer Methods in Applied Mechanics and Engineering* 51 (1985) 221–258.

[23] M. Petyt, Vibration of curved plates, *Journal of Sound and Vibration* 15 (1971) 381–395.

[24] M. Özakca, E. Hinton, Free vibration analysis and optimization of axisymmetrical plates and shells—I. finite element formulation, *Computers & Structures* 52 (1994) 1181–1197.

[25] R.L. Carter, A.R. Robinson, W.C. Schnobrich, Free vibration of hyperboloidal shells of revolution, *Journal of Engineering Mechanics Division ASCE EM2* 93 (1969) 1033–1053.

[26] B. Nayroles, G. Touzot, P. Villon, Generalizing the finite element method: diffuse approximation and diffuse elements, *Computational Mechanics* 10 (1992) 307–318.

[27] T. Belytschko, Y.Y. Lu, L. Gu, Element-free Galerkin methods, *International Journal for Numerical methods in Engineering* 37 (1994) 229–256.